Cryogenics 135 (2023) 103741

Contents lists available at ScienceDirect

Cryogenics

journal homepage: www.elsevier.com/locate/cryogenics

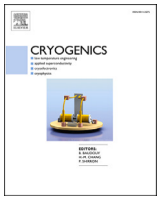

Research paper

Experimental study of three-phase helium mixtures in confined channels

Andrea Vitrano *, Vadim Stepanov, Gilles Authelet, Bertrand Baudouy

Université Paris-Saclay, CEA, Département des Accélérateurs, de la Cryogénie et du Magnétisme, Gif-sur-Yvette, 91191, Essonne, France

A B S T R A C T

An experimental campaign was conducted to investigate heat and mass transfer phenomena in superfluid helium (He II) in two rectangular cross-section channels of high aspect ratios and different thickness resembling the space between steel collars in the LHC superconducting magnets. The experiments consisted of clamped heat flux tests at atmospheric pressure, in which a heater strip suddenly releases a constant heat load into the channel that is open to a helium bath on one side. The difference in thickness between the two channels allowed exploring the effect of the geometrical confinement on the propagation of both phase change fronts: i) the He II-He I λ-transition front; ii) the He I-vapour first-order transition front.

The observations show that, in the thinner channel, it is possible to distinguish different behaviours of the phase fronts depending on the extent of the heat flux. For increasing heat flux values, the λ-front speed successively increases sharply, decreases, and increases weakly. This sequence is determined by the presence of the vapour film, which either diminishes the He II-He I transformation rate by lowering the heat transfer or pushes the λ-front while expanding. In the thicker channel, the intermediate behaviour is absent as the level of confinement is lower and the He I phase never expands considerably along the highest dimension of the channel.

1. Introduction

Superfluid helium (He II) is used as a thermal vector in the cooling system of superconducting magnet technologies because of its extraordinary heat extraction capability. The equivalent thermal conductivity of He II depends strongly on the magnitude of heat currents potentially present. In the heat flux range of magnet cooling applications, the thermal conductivity of He II is several orders of magnitude larger than metals [1], making it a unique coolant.

Despite the outstanding properties of He II, the confined structures surrounding superconducting magnet coils hinder significantly the cooling process. The cable electrical insulation tapes of the LHC magnet coils create a network of micro-channels in the range of 10 μm [2], which constitutes a thermal barrier between the He II stagnant bath and the coils. The necessity to improve the magnet cooling incentivized extensive studies to investigate the heat transfer taking place in such conditions, [3], [4], [5], [6] and come up with novel tape configurations that enhance the heat removal [7].

Another example of thermal barrier is represented by the steel collars, which are stacked in series along the LHC magnet dipoles and separated by spacings of about 200 μm [8]. An inefficient heat extraction at this level of confinement may cause a temperature increase in the coil, upon which the superconducting coil may quench [9]. Without effective quench protection measures, the event may result in high energy dissipation that vaporizes the coolant. The risk of such sudden events motivated a series of studies to understand magnet quench and prevent it [10], [11], [12], [13].

The phenomena arising in He II following high energy dissipation are yet to be clarified for geometrical confinements of few hundreds of microns. Unlike other fluids, helium has three different fluid states. Besides the already mentioned superfluid state (He II), helium can take the form of either an ordinary viscous liquid (He I) or a gas (helium vapour) depending on its thermodynamic conditions. It follows that there exist two phase transitions associated with helium as a fluid at atmospheric pressure: the λ-transition (He II-He I), which is a second-order transition, and the evaporation/condensation (He I-vapour), which is a first-order transition.

Depending on the amount of energy released in the He II contained in narrow spacings, one or both transitions can be triggered with consequent drastic changes in the thermophysical properties of the fluid. If we consider a one-dimensional channel of length L filled with static subcooled He II at an initial temperature T_b, it is possible to compute the minimum heat flux necessary to trigger the λ-transition (at the λ-point) by integrating the heat conductivity function f of He II over the range of temperatures between T_b and T_λ [1]:

$$q_{min} = \left(\frac{1}{L} \int_{T_b}^{T_\lambda} f^{-1}(T)\, \mathrm{d}T \right)^{\frac{1}{n}}, \tag{1}$$

* Corresponding author at: CERN, CH-1211, Geneva 23, Switzerland.
E-mail address: andrea.vitrano@cern.ch (A. Vitrano).

https://doi.org/10.1016/j.cryogenics.2023.103741
Received 11 June 2023; Received in revised form 30 August 2023; Accepted 1 September 2023
Available online 7 September 2023

Nomenclature

Roman letters

a	empirical coefficient	
c	specific heat capacity	$Jkg^{-1}K^{-1}$
D	hydraulic diameter	m
f	heat conductivity function	m^5KW^{-3}
g	gravitational acceleration	ms^{-2}
L	characteristic length	m
n	conductive heat power law coefficient	
q	heat flux	Wm^{-2}
T	temperature	K
t	time	s
v	velocity	ms^{-1}
x	position coordinate	m

Greek letters

α	thermal diffusivity	m^2s^{-1}
ρ	density	kgm^{-3}
σ	surface tension coefficient	Nm^{-1}
τ	thermal time constant	s

Dimensionless numbers

Bo	Bond number; $D^2 g\left(\rho_l-\rho_v\right)\sigma^{-1}$
Co	Confinement number; $Bo^{-\frac{1}{2}}$

Subscripts

λ	lambda point, lambda transition related
b	bath
He	helium
l	saturated liquid
p	constant pressure
v	saturated vapor

where n is a coefficient that depends on the temperature and ranges from 3 to about 4 around T_λ [14–16]. Some authors used 3.4, which is a good approximation in the range of temperatures between 1.7 K and T_λ [17]. In particular, Sato et al. performed a series of experiments at steady-state conditions to derive an accurate correlation for the heat conductivity function for $n = 3.4$ [18]. Above q_{min}, the fluid in contact with the heating surface will eventually undergo λ-transition. It is straightforward that the λ-time t_λ needed to achieve the λ-transition varies with the heat flux. Dresner derived a formula for t_λ as a function of the heat flux and temperature difference utilizing their own analytical method [19]:

$$t_\lambda = \frac{\overline{\rho c_p}\left(T_\lambda - T_b\right)^2}{(aq)^4\,\overline{f(T)}}, \tag{2}$$

where the thermophysical properties of He II are averaged in the range of temperatures between T_b and T_λ, while the proportionality constant a is equal to 1.16 [20]. The λ-time appears to depend strongly on the heat flux, decreasing with the fourth power of its reciprocal. Eq. (2) was validated experimentally with an agreement of 20% [1]. An equivalent equation for the λ-time was derived by Baudouy, who proposed a solution independent of experimentally fitted parameters [21]. Once t_λ is reached, a λ-front is formed close to the heating surface. The rate of transformation of He II into He I determines the way this front propagates throughout the channel. In the context of the superfluid recovery in helium-cooled conductors, Dresner was able to approximate the speed of the front v_λ as [22]

$$v_\lambda = \frac{\left[x_\lambda^{-1} f^{-1}(T)\left(T_\lambda - T_b\right)\right]^{\frac{1}{3}}}{\overline{\rho c_p}\left(T_s - T_\lambda\right)}, \tag{3}$$

where x_λ is the front position, T_s is the fluid temperature at the heating surface, and the properties of helium are averaged between T_s and T_λ.

As the heat flux is further increased, nucleate boiling phenomena take place until a vapour film arises at the peak nucleate boiling heat flux q^*. However, in confined geometries like narrow channels, the coolant volume is small and thus the heat removal due to convection and boiling is limited. As a consequence, q^* is much lower and the vapour film is easily established. It follows that, if He II undergoes λ-transition, the heat flux is likely to be large enough to trigger the first-order transition too [23], resulting in a stable triple-phase phenomenon [24], [25].

The goal of this work consists of unravelling the fundamental thermal phenomena occurring in He II when subjected to high heat fluxes in thin geometries with high aspect ratios, resembling the space between the collars. The study focuses on the heat and mass transfer of superfluid helium as well as the other fluid phases of helium. In particular, a wide range of heat fluxes will be tested to investigate the evolution and propagation of the helium phase transitions.

2. Experimental setup

The experimental rig needed to conduct the tests is presented in this section along with the main components and sensors utilized. The tests are carried out within a cryostat capable of keeping the temperature at values below 2 K. The experimental setup is constituted by solid components arranged together to form a thin channel, which is submerged in He II in horizontal position during the tests. The vertical position of the channel was also tested during another experimental session, which is not herein reported to preserve the scope of this study and can be found in [26].

The cryostat used for the experiments is a typical Claudet cryostat [27], which allows conducting the tests in a pressurized He II bath rather than at saturated conditions. This is particularly useful for the goal of the present study as the stagnant bath that surrounds the dipoles of the LHC is pressurized. The cryostat is constituted by an outlying stainless steel shell and two copper vessels. The outer vessel is separated from the shell by two radiation shields that minimize the radiative heat fluxes from the ambient condition of the laboratory. The outer vessel is connected to a pumping system that allows regulating the pressure inside the vessel containing saturated He II that is used to cool the inner vessel (see [26] for a detailed description of the cryostat and its components). The inner vessel is the actual test environment that accommodates the setup, which is fixed to a support frame equipped with an insulating G10 plate (also called λ-plate), four radiation shields, and an upper metal flange that serves to seal the cryostat when the frame is placed inside it. The λ-plate is a thermal insulation that separates the two helium baths in the inner vessel (see Fig. 1). The experiment takes place in the lower bath ($\approx$ 12.3 L) in pressurized He II, which hence must be cooled down below the lambda point.

The experimental setup is designed to form the desired geometry, which is meant to resemble the space in between the collars surrounding the superconducting coils. The concept of the experiment is represented in Fig. 2. He II fills a thin channel that is open to the bath of the experimental environment on one extremity and closed on the other by a heating source. The channel is enclosed by thick solid pieces that insulate thermally the He II contained in the channel from the bath. The heat source is supposed to dissipate energy only inside the channel. This preferential direction of the heat flux is obtained by means of an insulating plug posed behind the source and attached to the other

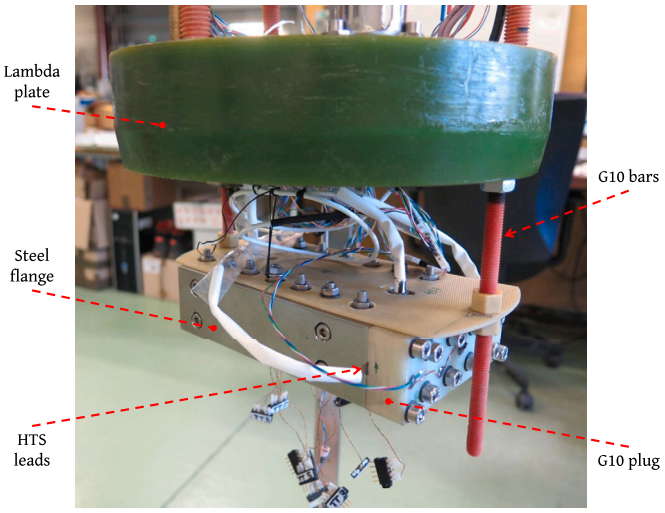

Fig. 1. Channel setup anchored to the frame bars in horizontal position.

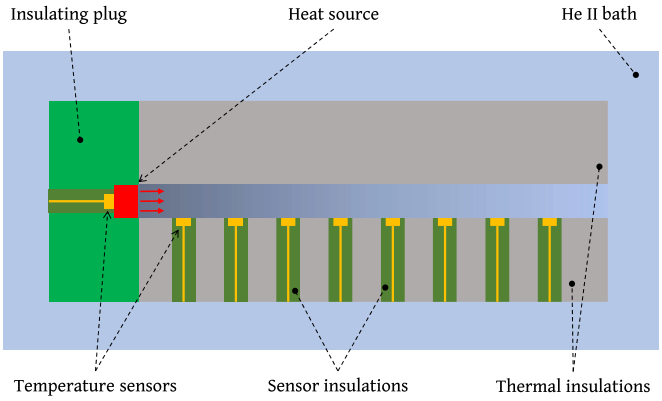

Fig. 2. Channel experiment concept representation.

solid parts. Several sensors mounted on the solid pieces will provide information about the temperature of the He II in the channel.

The setup, shown in Fig. 3, is constituted by five main components: two stainless steel plates, two side stainless steel flanges, and one G10 support. These five pieces are assembled together in order to shape a rectangular cross-section channel. The relative position of all the pieces is fixed and ensured by several stainless steel screws covered with vacuum grease, which does not crack at cryogenic conditions. One of the metal plates is machined on the central part of one surface to house the channel, which emerges when the other plate is put in contact with the machined one. These two plates are placed between the two side flanges, which minimize lateral leaks. Vacuum grease is inserted in the space between the main pieces, with particular attention to the contact surface of the two plates in order to not obstruct the channel zone with impurities to serve as sealant. The channel is 14 cm long and 5 cm wide, whereas its thickness is determined by the machined surface. Since the thickness is one of the study parameters, two machined plates were prepared in order to produce two channels of different thicknesses: 0.5 mm and 0.2 mm. Both plates are 2 cm thick and the overall side metal thickness (side flange plus unmachined plate portion) is 2.25 cm per side. Because of the small confined space inside the channel, a rough surface could affect the fluid motion. The stainless steel ensures the smoothness of the surfaces in contact with helium. The G10 support stands for the heater plug previously mentioned and is 2 cm thick. The G10, which is fiberglass, was selected as a plug material to ensure high thermal and electrical insulation for the heater. The surface of the plug that faces the helium channel is grooved to house the heating source, which was chosen to be a resistive wire made out of Manganin® [28] that allows producing Joule heating through electric currents. The wire is as thick as the channel and as long as the width of the channel, which means that the heater matches entirely one side of the channel. The uniform temperature distribution in the heated wire was verified by comparison with numerical models [23]. The extremities of the wire are soft-soldered to high-temperature superconductive (HTS) current leads on each side of the channel. The HTS leads, made out of a YBCO compound, prevent heat dissipation outside of the channel even in the case of helium evaporation by maintaining superconductivity at high temperatures. These tapes together with the heater are glued to the grooved surface of the plug with a polymerized epoxy resin (3M Scotch-Weld DP190) (see Fig. 4). The HTS leads, which are located between the side flanges and the plug, are in turn soft-soldered to NbTi superconducting wires with gold connectors to reduce the heat deposition in the pressurized helium bath. The current led by the NbTi wires to the heater is provided externally by a Tektronix® PWS4305 DC [29] power supply.

The channel setup is equipped with nine temperature sensors. Due to the size of the channel and the consequent small amount of helium contained in it, the temperature sensors are required to have a small size and thermal mass. For this reason, bare chip Cernox® CX-1050-BC temperature sensors with a sapphire base are adopted to ensure fast thermal response (1.5 ms at 4.2 K). Eight of them are inserted in appropriate holes machined in one of the steel plates. Their position in the holes is fixed by gluing them with epoxy resin to G10 supports, which also serve the purpose of electrically and thermally insulating the sensors from the metal plate. The supports are placed inside the holes so that the sensors are situated on the internal edge of the plate in direct contact with the helium, without altering the thickness of the channel at the hole location. The eight sensors are distanced 1.5 cm from each other along the centerline of the unmachined plate and the closest sensor to the heater is 1.5 cm far from it. This means that the farthest sensor from the heater is 2 cm far from the aperture of the channel. The ninth temperature sensor is meant to measure indirectly the temperature of the heater. Because of the small thickness of the wire, it was not possible to make a measurement with a sensor in direct contact with it. Therefore, a workaround, shown in Fig. 5, was conceptualized and implemented. Inside a hole in the G10 support, a small high purity copper rod is put in direct contact with the heater. This rod is machined such that a bigger hollow part expands the measurable surface. Finally, the sensor is glued inside the hollow part at a total distance of 2.8 mm from the heater.

The nine bare chip Cernox® sensors are not provided by the constructor along with a calibration curve. Therefore, they were calibrated in absence of heat loads against a Cernox® CX-1050-SD temperature sensor installed in the insert and situated near the aperture of the channel. The calibration data was collected from 1.5 K up to ambient temperature with the channel in the horizontal position in order to minimize temperature stratification effects. Each bare chip is built-in with the 4-wire resistance-temperature-detector (RTD) technique, which ensures accurate measurements by fully compensating for the resistance error due to the wires. According to this technique, the current to power the resistor is delivered through one pair of wires, and the actual voltage drop is measured through the other pair of wires. The sensors are powered with 10 μA delivered by a battery system.

2.1. Heat leaks

Despite this experimental setup is meant to provide information about the thermal response of He II, the interaction between helium and the various components surrounding it cannot be ignored. If He II undergoes phase transitions, its thermal time constant becomes comparable with one of the solid components and, thus, heat leaks from the channel through the materials start to be significant. Therefore, an analysis of the heat losses is presented to estimate the amount of energy that is not dissipated in helium. First off, the thermal time constant $\tau = L^2/\alpha$,

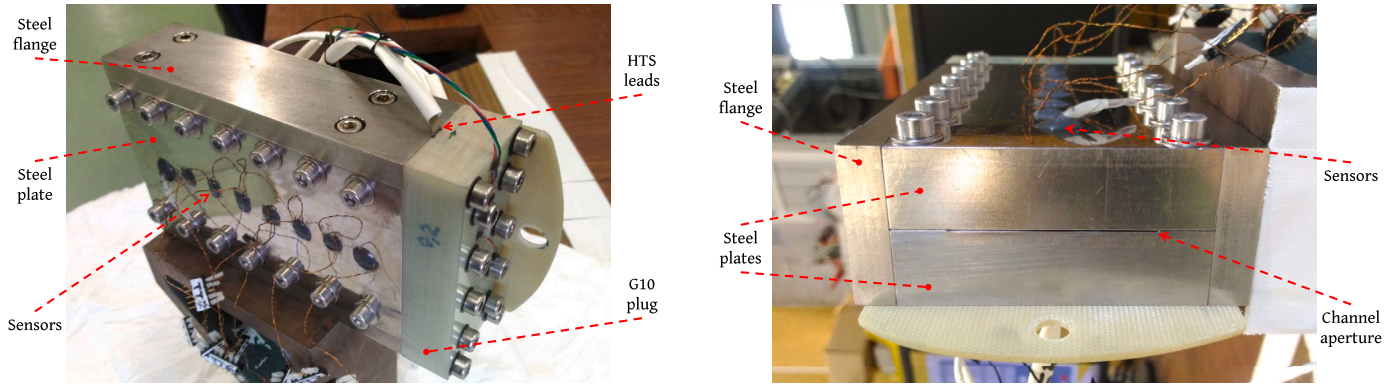

(a) View on the heater plug and temperature sensors plate

(b) View on the 0.5 mm thick channel aperture

Fig. 3. Channel assembly.

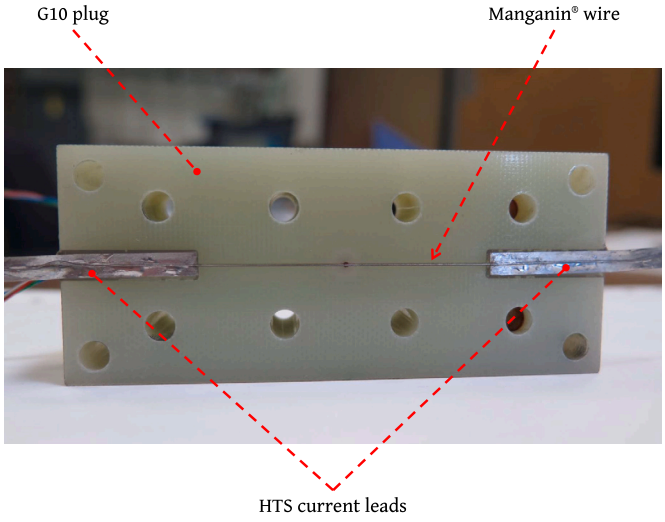

Fig. 4. 0.5 mm thick Manganin® wire soft-soldered to the HTS current leads and glued on the G10 heater plug.

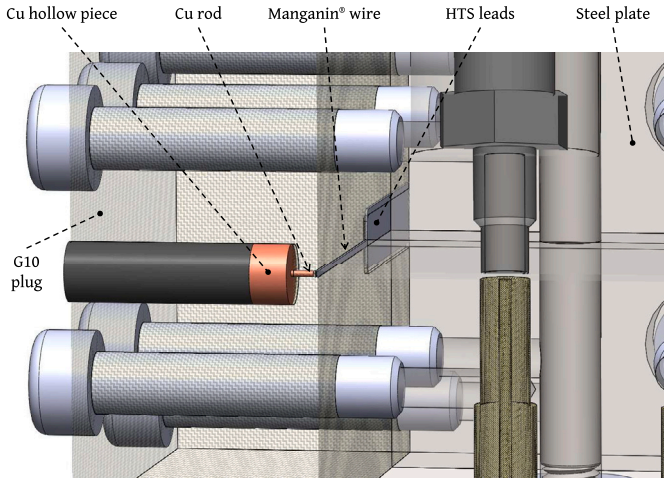

Fig. 5. Temperature measurement design for the heating wire.

defined as the ratio between the square of the characteristic length L and the thermal diffusivity α of the material, must be evaluated for the main leak paths of the setup. Components with a low time constant suffer fast temperature changes, which affect the steady-state temperature profile of helium. Fig. 6 reports τ as a function of the temperature

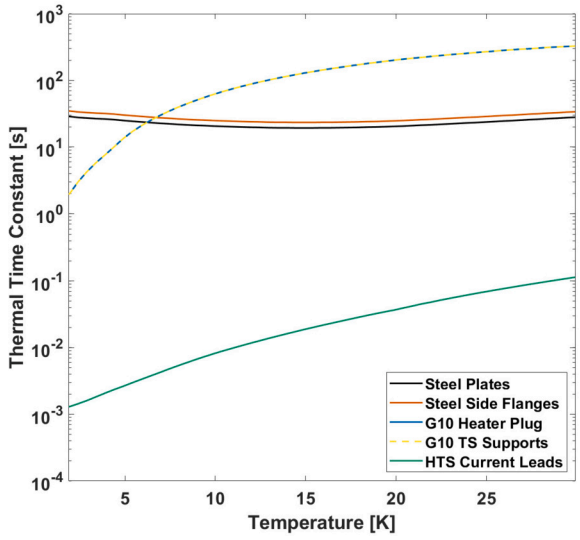

Fig. 6. Thermal time constants of the experimental setup components.

for different components. The time constant of the HTS current leads is several orders of magnitude lower than the other materials because of its high thermal conductivity. On the other hand, the G10 components (temperature sensor supports and heater plug) have very high τ.

The heat losses are computed via one-dimensional integration of the thermal conductivity of the material for different ranges of temperature starting from the reference value 1.9 K and taking into account the area of contact with the helium in the channel. The total heat losses are presented in Fig. 7 for both channel thicknesses. More specifically, Fig. 7 shows the heat loss as a percentage with respect to the heat applied through the heater. Since the heat loss increases with the temperature, the zone that experiences the highest losses is the one nearby the heater. For this reason, the contact surface of the steel parts is taken as the area from the heater to the first sensor. Taking into account that 10% is an acceptable loss, the heat leaks become significant above 5 K for an applied heat flux equal to 30 kW/m^2 and 15 K for 480 kW/m^2. It must be borne in mind though, that these values refer to the steady state and hence have an actual impact only for test durations comparable with the thermal time constant of the materials.

The experimental setup was also modelled numerically to verify the heat transport phenomena recorded [23].

3. Experiments

This section reports the data from the experimental sessions conducted with the channel setup described above. In the following figures,

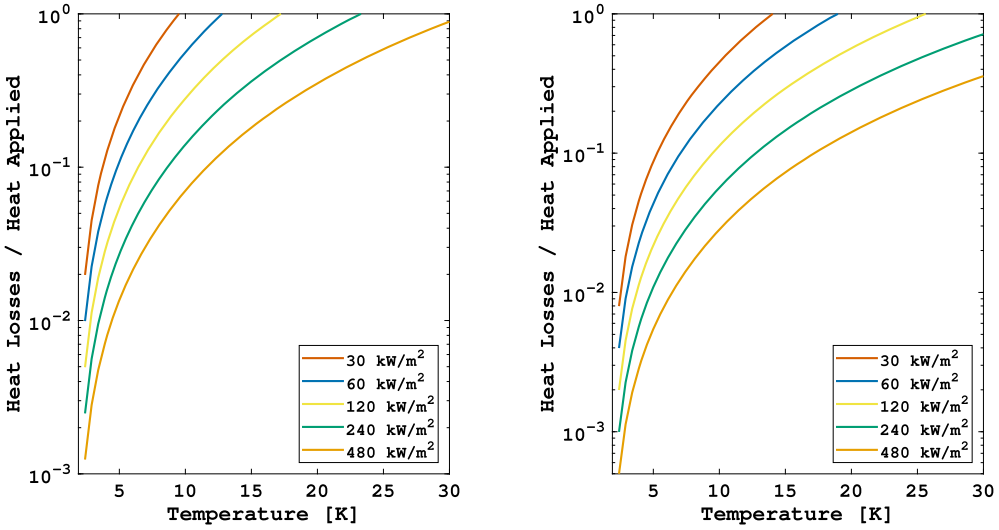

(a) 0.2 mm thick channel (b) 0.5 mm thick channel

Fig. 7. Total heat losses estimation as a function of temperature for different representative heat fluxes.

the temperature sensors are labelled as "TSX", where X is a digit that is proper of a specific sensor. TS9 is the sensor situated in the heater plug, behind the Manganin® strip, while for the sensors installed in the steel plate (see Fig. 2) X goes from 1 (closest sensor to the heater) to 8 (closest sensor to the channel aperture). Various tests were carried out with different heat fluxes and bath temperatures T_b. The experiments consist of the so-called clamped flux tests, where a constant heat flux is applied on the closed side of the channel by providing electric current to the resistive strip (i.e., the heater). The energy produced by the heater via Joule effect divided by the contact area with the helium contained in the channel determines the equivalent heat flux applied. If the heat flux applied in the channel overcomes the minimum heat flux q_{min} (Eq. (1)), He II undergoes λ-transition. Depending on the extent of the heat flux and its application time, the He II-He I transformation may propagate along the channel. Experimental results obtained with greater heat fluxes than q_{min} are reported and discussed in this study to investigate the phase transitions of helium.

3.1. Clamped flux tests

Fig. 8 shows the temperature evolution of helium following the application of a clamped flux in the 0.2 mm thick channel for different heat fluxes and a bath temperature of 1.9 K. At a heat flux moderately above q_{min} (Fig. 8a), the lambda transition does not occur beyond 3 cm from the heater. After the initial temperature increase at the TS1 location, the second time derivative of the temperature changes sign before reaching the steady state because of the increasing temperature gradient close to the heater. Once the λ-point is reached, the temperature rises sharply as He II turns into He I. The distinct change in slope of the temperature evolution can be explained by considering that the specific heat c_p of helium at the λ-point at atmospheric pressure is more than seven times higher than at 2.2 K [1], raising the temporal partial derivative of the temperature in the one-dimensional diffusion equation ($\partial T/\partial t = (\rho c_p)^{-1}\partial q/\partial x$). The steady state is reached after 20 s, when the temperature at TS1 is stable in He I with temperature oscillations within 0.2 K.

As the heat flux applied is raised (Fig. 8b), the λ-front propagates downstream and stops at around 4 cm far from the channel aperture. It is clear that helium vapour is generated close to the heater, as the temperature at TS1 fluctuates around 4.7 K after overcoming a plateau at the boiling point. The He I region seems to extend over a great portion of the channel, which grows with the heat flux covering an increasing number of sensors. It can be noticed that in the early moments of the transient the temperature at TS2 is higher than at TS1. This is not a heat diffusion phenomenon as it would be witnessed also without phase transitions. It is rather caused by the distribution of the vapour and He I phases in the channel. It must be taken into account that the channel is 5 cm wide and hence the expanding phases are likely to be distributed non-uniformly in horizontal position. When the bubbles are produced in the vicinity of the heater, they develop downstream heterogeneously and end up being confined in certain regions by the surface tension forces and thickness of the channel. Eventually, their proximity to the sensors determines the irregular temperature gradient.

At higher heat fluxes (Figs. 8c and 8d), the temperature fluctuates markedly between 7 K and values just above the saturation one. Remarkably, increasing the energy dissipated does not cause the λ-front to propagate farther in the channel. The temperature crosses the λ-point within 10 s since the application of the clamped flux and returns to the superfluid range after a few seconds. This is observed at multiple sensor locations with greater heat fluxes. Moreover, the λ-front reaches fewer sensors as the heat flux rises. This phenomenon is the consequence of a vapour film generated quickly at the heater surface. The higher the heat dissipated, the sooner the onset of the film boiling regime. Since the thermal conductivity of helium vapour is considerably low, the film acts as an insulator and increases the temperature gradient. For the same reason, the steady-state temperature at TS1 in Fig. 8d is lower than in Fig. 8c.

At very high heat fluxes (Figs. 8e and 8f), the amount of vapour generated is such that, after the initial increase, even at TS1 the temperature decreases almost below the λ-point before rising again. Moreover, the temperature at TS2 is no longer higher than the one recorded by TS1 in the early transient, as the vapour region occupies a greater portion of the channel and develops homogeneously throughout it. The He I region is now limited to a small portion of the channel (i.e., less than 1.5 cm), as the temperature at TS3 remains in the He II range until steady state. The inset in Fig. 8e reveals the temporary increment of the temperature due to diffusion in the whole channel at the very beginning of the transient. Once the vapour film is generated, the temperature drops before starting a slow growth that will bring helium at TS2 to change phase twice at a much later stage of the test — after 10 s. A bump that reaches 10 K happening above the boiling point is observable in both Figs. 8e, 8f. A similar bump is also present in Fig. 8f at TS2, which occurs right after the one recorded at TS1. This might be due to a vapour region propagating quickly after the heat impulse and collapsing as it travels through the channel.

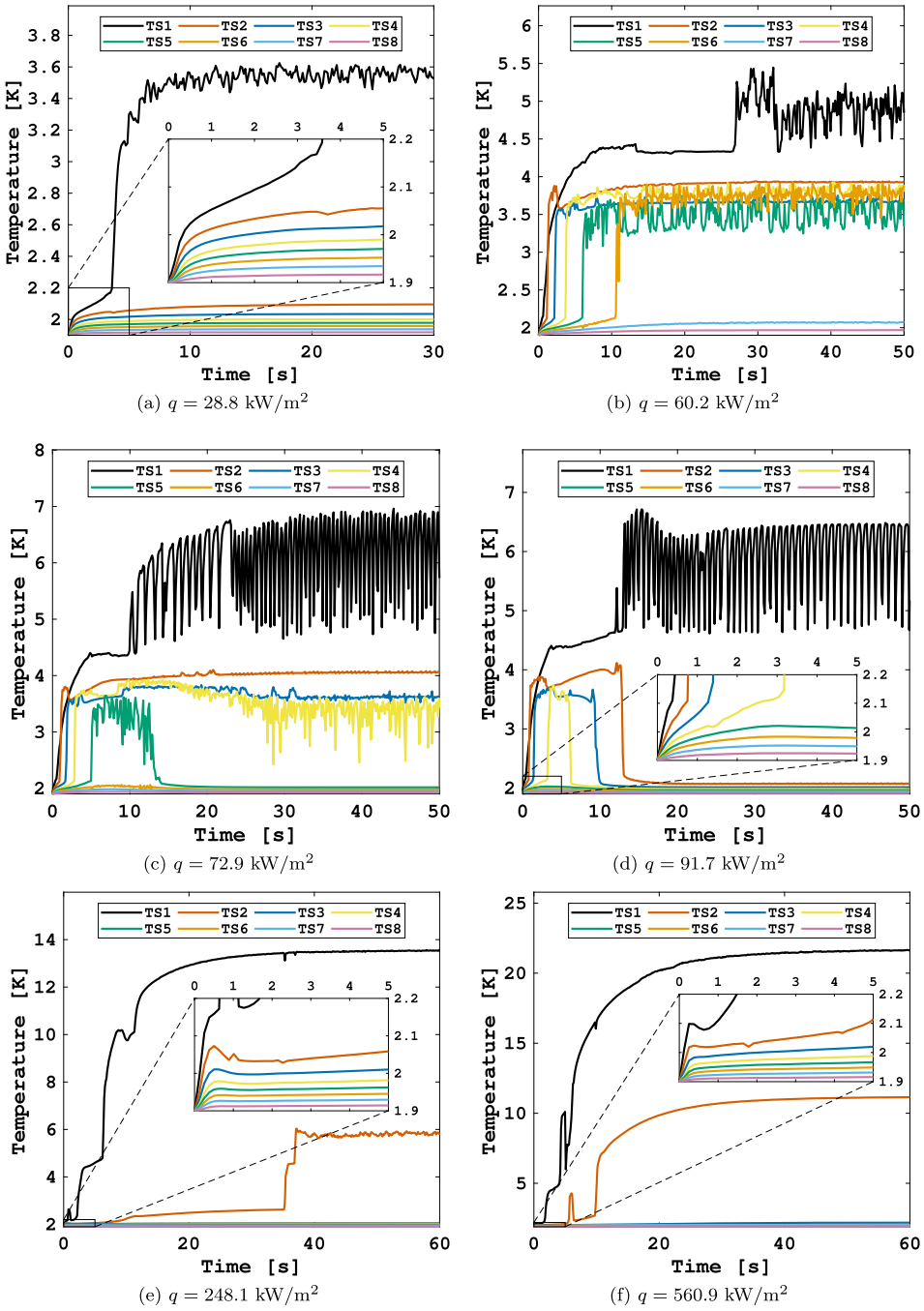

(a) $q = 28.8$ kW/m^2 (b) $q = 60.2$ kW/m^2

(c) $q = 72.9$ kW/m^2 (d) $q = 91.7$ kW/m^2

(e) $q = 248.1$ kW/m^2 (f) $q = 560.9$ kW/m^2

Fig. 8. Temperature evolution in the 0.2 mm thick channel at $T_b = 1.9$ K and different heat fluxes q.

3.2. Effect of the channel thickness

The clamped flux tests were repeated in the 0.5 mm thick channel in order to see the effect of a larger geometry on the phase change phenomena. Before presenting the results, it is useful to make a few considerations through the usage of the confinement number Co, which is a measure of the restrictive effect of the confining geometry on the boiling flow. The Co number is defined as the square root of the Bond number (Bo) reciprocal:

$$Co = \frac{1}{\sqrt{Bo}} = \frac{1}{D}\sqrt{\frac{\sigma}{g(\rho_l - \rho_v)}}, \tag{4}$$

where D is the hydraulic diameter, σ is the surface tension coefficient, g is the gravitational acceleration, and ρ_l and ρ_v are the densities at saturation of the liquid and vapour phase respectively. The hydraulic diameter for rectangular channels is computed as $D = 4A/p$, where A and p are respectively the area and perimeter of the channel cross-section. Calculating the Co number at atmospheric pressure gives as result approximately the values 0.72 and 0.29 for the 0.2 mm and 0.5 mm thick channels respectively. Cornwell and Kew identified $Co = 0.5$ as the threshold that differentiates between confined and non-confined two-phase flows [30]. Above this value, the boiling flow is affected by the restricting geometry. Therefore, the propagation of the phase change fronts, when the vapour phase is present, is expected to differ significantly in the 0.5 mm thick channel compared to the smaller one.

Fig. 9 shows the temperature evolution in the 0.5 mm thick channel at $T_b = 1.9$ K. It is immediately clear from a comparison between Figs. 9a, 9b and Figs. 8a, 8b that the He I region is much thinner in

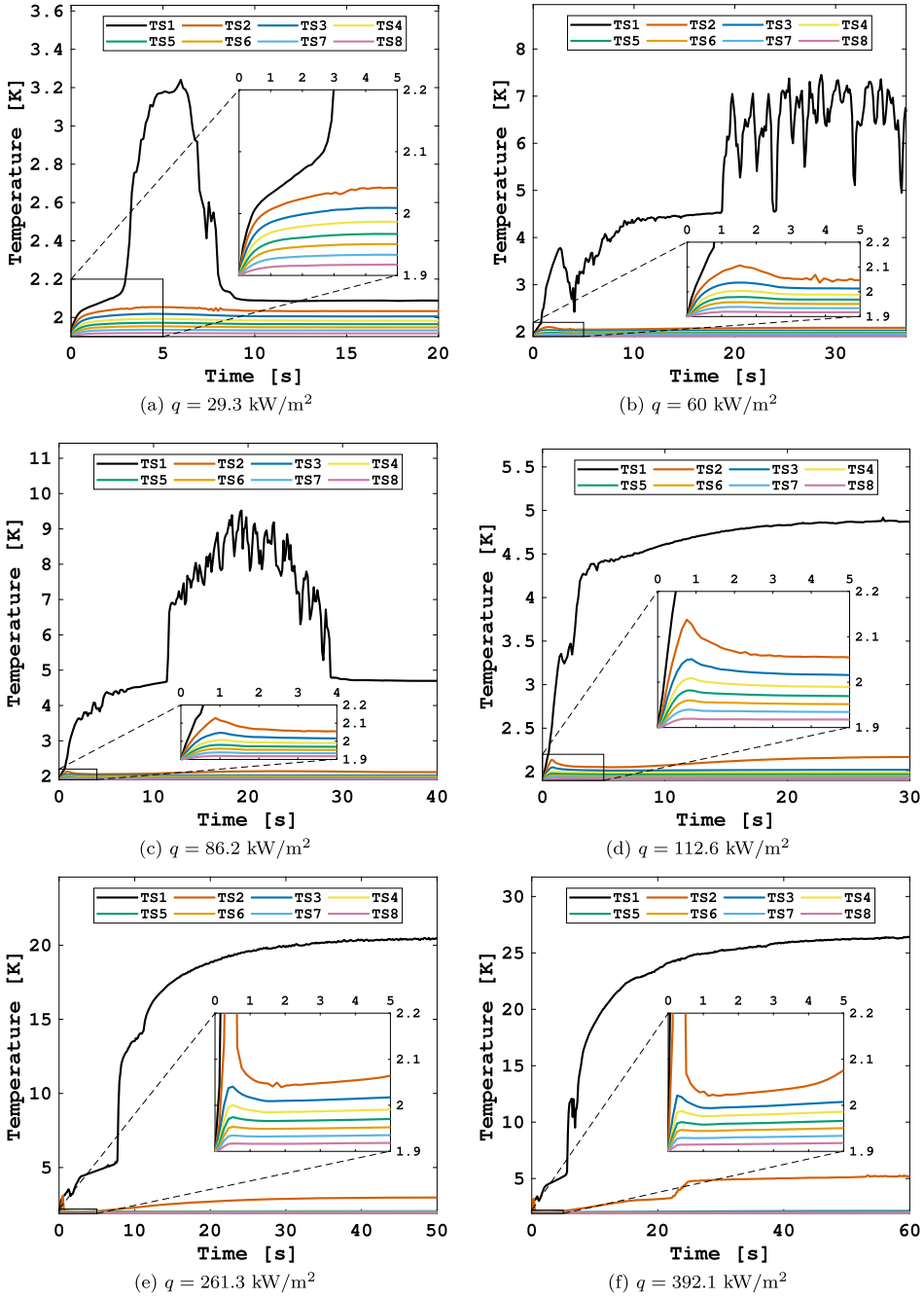

(a) $q = 29.3$ kW/m^2 (b) $q = 60$ kW/m^2

(c) $q = 86.2$ kW/m^2 (d) $q = 112.6$ kW/m^2

(e) $q = 261.3$ kW/m^2 (f) $q = 392.1$ kW/m^2

Fig. 9. Temperature evolution in the 0.5 mm thick channel at $T_b = 1.9$ K and different heat fluxes q.

the larger channel. In fact, with a heat flux moderately above q_{min}, the λ-front reaches TS1 before receding close to the heater. In Fig. 9b, the vapour-He I interface oscillates nearby TS1, while TS2 remains in He II until steady state. The He I phase is, thus, confined between the vapour and He II phases in a portion that is less than 1.5 cm long. All the other sensors register temperatures in the He II range of values. In contrast, in the same range of heat fluxes in the 0.2 mm thick channel, the λ-front crosses multiple sensors before receding close to the heater. This dissimilarity with respect to the smaller channel lies in the expansion of the liquid-vapour mixture, which occurs mostly horizontally because of space lacking in the direction of gravity.

At a higher heat flux (Fig. 9c), the maximum temperature at TS1 is greater than the steady-state one, which indicates a growing vapour film. This is confirmed by Fig. 9d, where the vapour phase is stable at TS1 at a temperature just above the saturation value and hence much lower than in Figs. 9b and 9c. After the first diffusion-driven increment, the λ-front develops slowly and approaches TS2. Raising further the heat flux (Figs. 9e and 9f) does not cause major differences in the temperature evolution. The heat diffusion is such that the λ-front passes TS2 within 1 s since the application of the flux. After dropping down below T_λ, the temperature at TS2 starts a slow growth with a resulting first-order phase change after 20 s (Fig. 9f).

It is important to underline a subtle distinction in comparison to the smaller channel. While in the 0.2 mm thick channel the first temperature increment seems to attenuate as the heat flux increases (Figs. 8e and 8f), in this case the time at which the temperature reaches T_λ appears constant (Figs. 9e and 9f). This will be confirmed by studying the λ-front speed, which is presented in the next section. It is also interesting to notice that, unlike in the smaller channel, the temperature at a sensor is always above the one at the next sensor (e.g., TS1 > TS2).

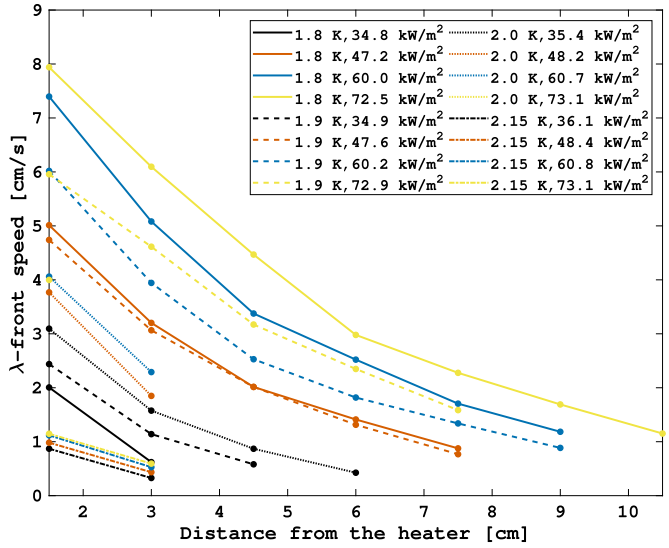

Fig. 10. Lambda front propagation along the 0.2 mm thick channel for different heat fluxes and bath temperatures. The circle markers indicate the position of the sensors.

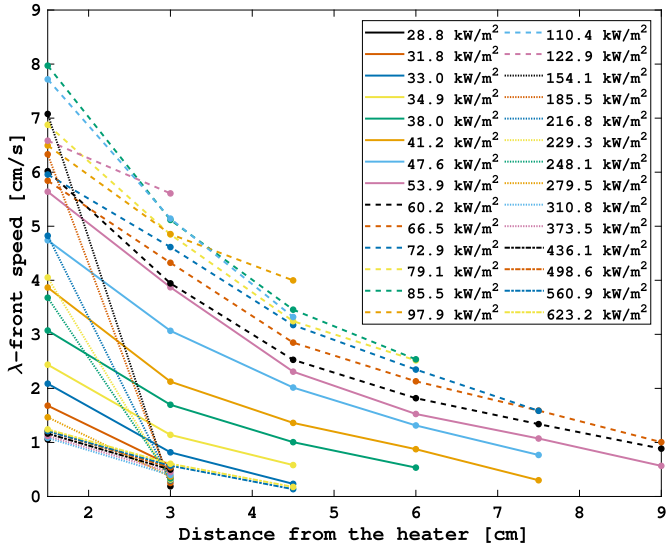

Fig. 11. λ-front propagation along the 0.2 mm thick channel for different heat fluxes at $T_b = 1.9$ K. The circle markers indicate the position of the sensors.

This confirms that the overlapping evolution seen in Fig. 8 is due to the size of the channel, which obstructs the homogeneous distribution of the vapour and He I phases.

4. Double-front propagation

The data collected from the clamped flux tests in the 0.2 mm thick channel provides information on the propagation speed of the λ-front. The speed is computed as the ratio between the distance from the heater to a certain sensor and a time difference. The latter is the difference between the time at which a sensor measures T_λ and the time at which the heater reaches T_λ. Fig. 10 is a comparison of the λ-front speed at four different bath temperatures among four heat fluxes in the range between 35 kW/m^2 and 73 kW/m^2. The solid, dashed, dotted, and dash-dotted lines refer to the speed profiles obtained respectively at 1.8 K, 1.9 K, 2 K, and 2.15 K. As predicted by various authors [22], [31], [32], the speed is inversely proportional to the front position. It is immediately clear that the lower the bath temperature, the wider the range of speeds covered in the same interval of heat fluxes. Both the speed and the path length traveled by the front increase with the heat flux. However, as the bath temperature approaches T_λ, the path shortens with the heat flux. At 2 K, the front barely reaches TS1 at the highest heat flux. This can be explained by considering the onset of film boiling. This is confirmed by the profiles at 2.15 K, which diverge from the other results by showing lower speed and slope, and a covered path independent of the heat flux. The initial temperature is evidently too close to T_λ for the He I phase to travel down the channel before the latent heat of vaporization is matched by the energy dissipated. It is legitimate to think, thus, that the λ-front propagation is affected by the vapour phase growth.

Fig. 11 shows the speed profiles for a larger range of heat fluxes at 1.9 K. As seen in the previous graph, the speed increases with the heat flux. This stops being valid at a certain heat flux (i.e., roughly 10^5 W/m^2), above which the speed starts decreasing with the heat flux. This effect is particularly clear beyond TS1 as indicated by the speed computed at TS2, where the value drops drastically above the aforementioned heat flux. Moreover, the path length traveled by the front does not vary for a wide range of heat fluxes: it is only at very high values that the front approaches TS3. Increasing the heat flux above 10^5 W/m^2 results in a gradual change in the slope of the profiles, which tends to resemble the behaviour already observed in Fig. 10 at 2.15 K. In this case, since the bath temperature is lower, more energy is required to trigger the first-order phase change in order to obtain this particular slope.

This variation of the front propagation is better visualized in Fig. 12, which shows the front speed as a function of the temperature difference between the heater and the He II bath for different heat fluxes. The results obtained at 1.9 K (Fig. 12a) and 2.15 K (Fig. 12b) are compared. The temperature dependence of the speed at a constant location in the channel is roughly linear at low and high temperatures (Fig. 12a). However, the function is much steeper for low differences in temperature. In the intermediate range of temperatures (i.e., between the two distinguishable linear trends for a specific sensor), the front appears to reach TS1 only, where the slope becomes negative and the function ceases to be linear. At locations from TS2 on, after the first linear function, the front is again detected at a much higher heater temperature, indicating that the phenomenologic change of the propagation occurs nearby the heater.

At 2.15 K (Fig. 12b), the differentiation can be identified for TS1 only. The steep function is visible just for very low temperatures, whereas above around 10^4 W/m^2 the speed increases at a slope similar to the high-temperature region of Fig. 12a. It appears clear at this point that the λ-front speed is greatly affected by the growing vapour film and boiling front.

The data of the front speed was utilized to study Eq. (3), which was derived by Dresner to approximate the λ-front speed [22]. For this purpose, a proportionality factor K is introduced and defined as

$$K = \frac{v_\lambda \overline{\rho c_p}\left(T_s - T_\lambda\right)}{\left(x_\lambda^{-1}\int_{T_b}^{T_\lambda} f_S^{-1}(T)\,\mathrm{d}T\right)^{\frac{1}{3.4}}}, \tag{5}$$

where v_λ and x_λ are the speed and position of the front, T_s is the heater temperature, and density and specific heat are averaged in the temperature range between T_λ and T_s. In Dresner's formula, which is applicable to He II-He I multiphase cases, the factor K would equal 1 assuming that using averaged properties is a correct assumption. Any deviation from unity would then indicate either the inaccuracy of the assumption or a different multiphase regime (e.g., presence of helium vapour at the heating surface). Computing K at every sensor location with the present data reveals that K depends on the heat flux. Fig. 13 shows that K varies from 0 to 3 below 10^5 W/m^2. Above this value, when the vapour phase is stable at the heater, K drops down below 1. In this region, K depends markedly on the front position and varies weakly with the heat flux. Averaging the properties represents no longer a correct

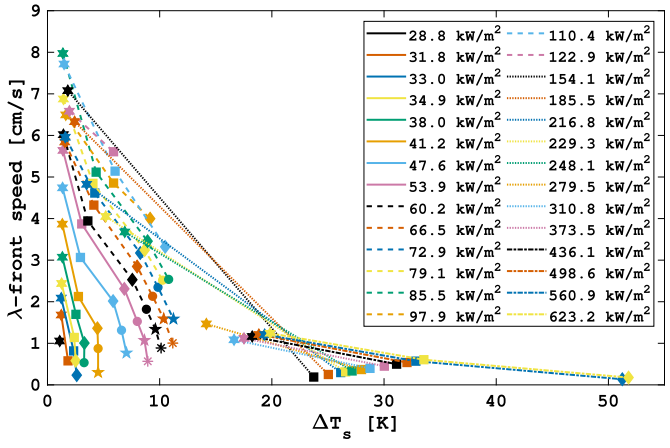

(a) $T_b = 1.9$ K

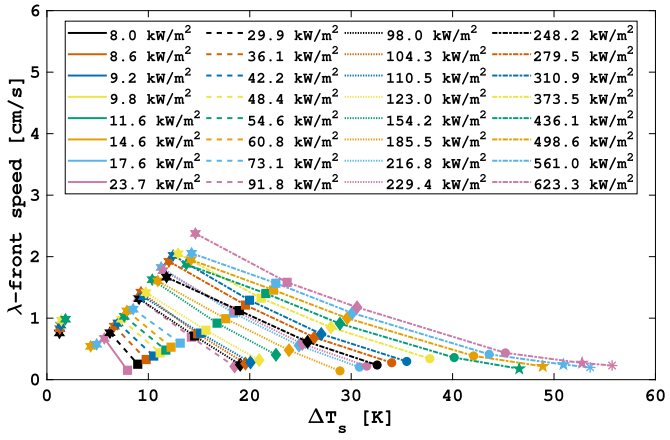

(b) $T_b = 2.15$ K

Fig. 12. λ-front speed with respect to the temperature difference between the heater and bath for different heat fluxes. Each sensor location along the channel is referred to with a different marker: from TS1 to TS6 the markers are respectively hexagrams, squares, diamonds, circles, pentagrams, and asterisks.

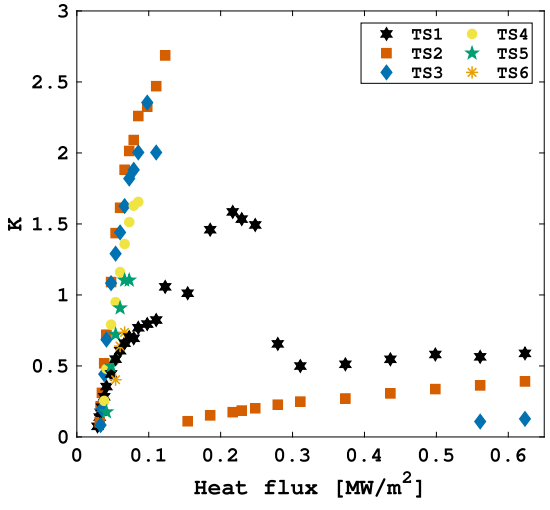

Fig. 13. Proportionality factor K as a function of the heat flux for different positions of the λ-front in the 0.2 mm thick channel at 1.9 K.

assumption as the density lies between the values of vapour and He I, decreasing considerably the value of K.

At last, it is interesting to compare the lambda and boiling fronts with each other at the location where the most data is available (i.e., TS1). Fig. 14 presents this comparison as a function of the heat flux for both channels, which are labelled according to their confinement number. In the 0.2 mm thick channel (Fig. 14a), three different regions are clearly distinguishable for the λ-front speed. In the first one, the speed increases sharply with the heat flux until around 10^5 W/m^2, where a peak is reached. In the second region, the speed drops at a similar rate down to the value of the first detectable front. Thereafter, the speed becomes weakly proportional to the heat flux. On the other hand, the boiling front travels at a much lower speed and never overcomes 1 cm/s. Its speed increases slowly until 10^5 W/m^2, after which a small drop occurs. Then, the speed rises at the same rate of the λ-front. To sum up, this figure clarifies the mechanism of double front propagation in He II. The λ-front travels at a speed that is proportional to the heat flux until the boiling front reaches its maximum value. As the heat flux increases, the time to achieve the film boiling regime diminishes and the temperature gradient rises earlier. As a result, the He II-He I transformation rate decreases, and thus the He I phase thins. The λ-front speed is then determined by the vapour phase growth, with the two fronts propagating at the same rate.

In the 0.5 mm thick channel (Fig. 14b), the boiling front presents similar characteristics. However, only two regions can be distinguished for the λ-front. The first one is comparable to the case of the smaller channel. The second region resembles the third one in Fig. 14a, where the speed rate looks like the boiling front one. Nevertheless, the speed is greater than in the previous case. The intermediate region characterized by a speed drop is no longer present, which explains the absence of attenuation in the first temperature increment (see Sec. 3.2). Since the confinement number is lower than the critical value, the vapour and He I phases expand more easily, ensuring a relatively high λ-front speed in the last region. Another difference lies in the number of times the λ-front travels through the same spot. Because of the early peaks detected in multiple tests (see Fig. 9), it is possible to identify two λ-fronts. The primary front is the diffusion-driven one, similarly to the smaller channel. The secondary one is associated with speeds in the range of the boiling front. This result confirms that the nature of slow λ-fronts is mainly due to the vapour-He I transformation process, which is also responsible for preventing the λ-front speed to increase with the heat flux for non-confined channels.

5. Conclusions

The present study investigates heat and mass transfer phenomena in superfluid helium in two rectangular cross-section channels of high aspect ratios. The experiments consisted of clamped heat flux tests at atmospheric pressure, in which the heater releases a heat load into the channel. The difference in thickness between the two channels allowed exploring the effect of the geometrical confinement on the propagation of the phase change fronts in the presence of helium vapour. The conclusions of this study are summarized below.

Applying clamped heat fluxes above the lambda critical value triggers the second-order phase transition, which causes a sudden temperature increase due to the abrupt drop in specific heat capacity from He II to He I.

In thin channels of high aspect ratios the minimum heat flux needed to trigger the second-order phase transition is sufficiently large to initiate boiling too. At the saturation temperature, the fluid mixture temperature experiences a steady evolution due to the latent heat of vaporization. The duration and slope of this evolution are affected by the heat flux: the higher the heat flux, the shorter and steeper the evolution at a certain location.

Considerably different steady-state temperature profiles can be distinguished in the confined channel depending on the heat flux applied.

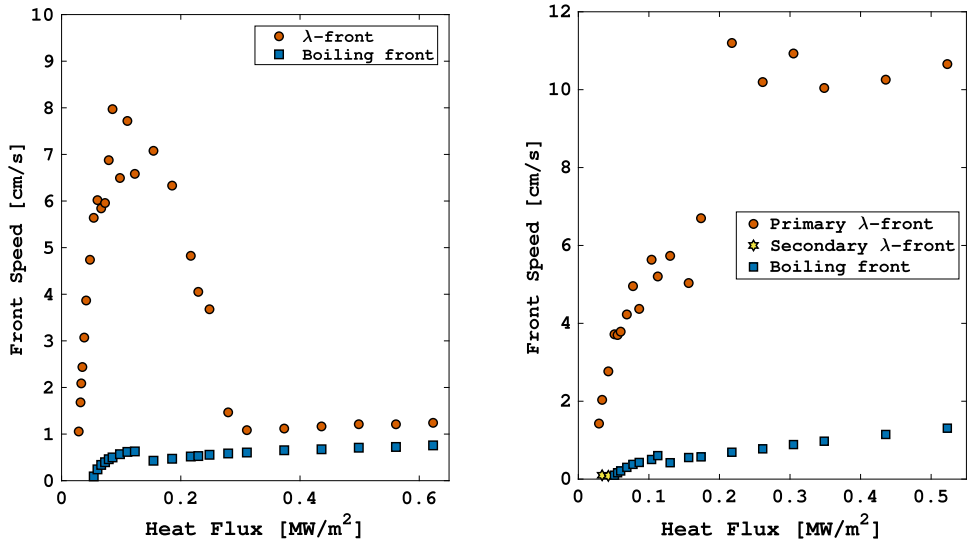

(a) $Co > 0.5$ (b) $Co < 0.5$

Fig. 14. Speed of the lambda and boiling fronts at 1.5 cm far from the heater as a function of the heat flux applied at a bath temperature of 1.9 K.

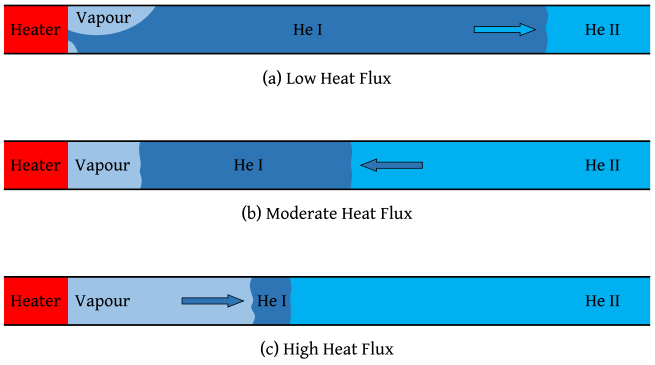

(a) Low Heat Flux

(b) Moderate Heat Flux

(c) High Heat Flux

Fig. 15. Representation of different multiphase regimes according to the extent of the heat flux applied.

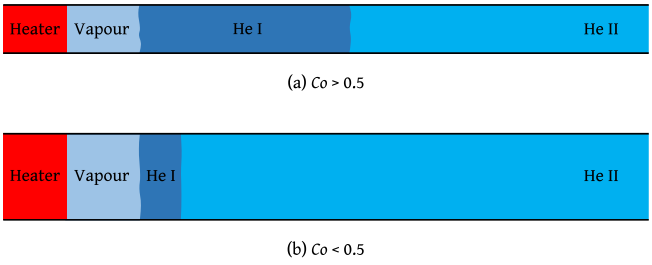

(a) $Co > 0.5$

(b) $Co < 0.5$

Fig. 16. Representation of different multiphase configurations according to the confinement number Co.

By qualitatively subdividing the heat fluxes into low, moderate, and high values, three different phenomenologic zones can be distinguished. Increasing the heat flux has different effects within each zone (see Fig. 15): the He I phase occupies an increasing portion of the channel, while helium vapour is confined next to the heater (low q zone); the He I region progressively shortens after an initial expansion and He II returns to occupy the majority of the channel (intermediate q zone); the He I phase occupies a small portion of the channel between He II and the expanding vapour phase (high q zone). These opposing behaviours are due to different multiphase regimes. At low heat fluxes, the vapour phase is heterogeneously constituted by small regions that allow maintaining a direct thermal link between the heater and He II. As a consequence, the He II-He I transformation rate grows proportionally to the heat flux and, hence, the He I phase expands quickly. At moderate heat fluxes, the vapour regions slowly coalesce into a homogeneous insulating film that blankets the heater (i.e., film boiling) and makes the temperature gradient increase. It follows that the λ-front propagation slows down and stops earlier before receding because of the heat removal from the He II bath. At high heat fluxes, the onset of film boiling takes place so rapidly that the He II-He I transformation is hindered since the beginning of the transient. The vapour phase expands then proportionally to the heat flux.

At high heat fluxes, a bump-like temporary temperature increment is always observed at the beginning of the clamped flux tests. This increment decreases towards the bath but occurs at the same instant at every location of the channel. As such, it has been attributed to a diffusion-driven temperature rise that stops at the onset of film boiling, when the temperature drops back within the He II range. The peak of the bump decreases with larger heat fluxes until it disappears.

The thickness of the channels determines the relative proportion between the different phases of helium. In contrast to the 0.2 mm thick channel, in the thicker channel the He I phase does not cover a large portion of the channel regardless of the heat flux (see Fig. 16). Therefore, the thinner the channel, the more the He I phase expands longitudinally. It can be concluded that the thickness of the He I region decreases with increasing characteristic dimensions of the geometry until it reaches a minimum value determined by He II and vapour.

If the temperature is sufficiently lower than T_λ and the heat flux is moderately low (i.e., below 10^5 W/m^2), the λ-front speed is inversely proportional to the front position in the channel. However, if the temperature is in close proximity to T_λ or the heat flux is too large, the slope of the speed profile changes, altered by the growing vapour phase.

In the confined channel, at a constant location not far from the heating surface, the λ-front speed varies differently according to the heat flux range. With reference to the categorization previously introduced, it is possible to distinguish three main zones: the speed increases sharply with the heat flux (low q zone); the speed decreases with increasing heat flux (intermediate q zone); the speed increases weakly with the heat flux (high q zone). Since in the moderate zone the λ-front propagation slows down and stops earlier, this zone is absent at locations farther from the heater. Because of the change in behaviour from the low zone to the intermediate one, there exists a top speed and a maximum length covered by the front.

The boiling front travels much more slowly than the λ-front. Unlike the latter, the boiling front shows two behavioural zones only: the speed increases with the heat flux with a negative second derivative until a

maximum value (first zone); the speed increases weakly with the heat flux at the same rate as the λ-front (second zone). The first zone matches roughly the λ-front low zone. Since the second zone corresponds to both the moderate and high λ-front zones, the similar growth rate in the second zone indicates that the λ-front propagation is mainly determined by the expansion of the vapour phase and hence of the boiling front propagation.

Different levels of geometrical confinement affect significantly the relationship between the λ-front speed and heat flux. In the non-confined channel, only two zones are distinguishable: the speed increases sharply with the heat flux (low zone); the speed varies weakly with the heat flux (high zone). Since the level of confinement is lower, the vapour and He I phases expand more easily and, thus, the λ-front speed in the high zone is greater than the top value reached in the confined channel.

Because of the diffusion-driven temperature increase in the early moments of the transients, the λ-front may cross the same location in the channel twice. The primary front is diffusion-driven and travels at a typical λ-front speed, while the secondary front is due to the vapour expansion and travels at a typical boiling front speed.

CRediT authorship contribution statement

We confirm that the manuscript has been read and approved by all named authors and that there are no other persons who satisfied the criteria for authorship but are not listed. We further confirm that the order of authors listed in the manuscript has been approved by all of us. We confirm that we have given due consideration to the protection of intellectual property associated with this work and that there are no impediments to publication, including the timing of publication, with respect to intellectual property. In so doing we confirm that we have followed the regulations of our institutions concerning intellectual property.

Declaration of competing interest

The authors declare that they have no known competing financial interests or personal relationships that could have appeared to influence the work reported in this paper.

Data availability

Data will be made available on request.

Acknowledgement

This research was mainly supported by EASITrain – European Advanced Superconductivity Innovation and Training. This Marie Skłodowska-Curie Action (MSCA) Innovative Training Networks (ITN) received funding from the European Union's H2020 Framework Programme under grant agreement no. 764879. The authors would like to thank the CERN CryoLab and Rob Van Weelderen for proposing and supporting forward-looking experiments through a CERN-CEA collaboration.

References

[1] Van Sciver SW. Helium cryogenics. New York: Springer; 2012.
[2] Meuris C, Baudouy B, Leroy D, Szeless B. Heat transfer in electrical insulation of LHC cables cooled with superfluid helium. Cryogenics 1999;39(11):921–31. https://doi.org/10.1016/S0011-2275(99)00115-0.
[3] Baudouy B, François M, Juster F-P, Meuris C. He II heat transfer through superconducting cables electrical insulation. Cryogenics 2000;40(2):127–36. https://doi.org/10.1016/S0011-2275(00)00015-1.
[4] Richter D, Fleiter J, Baudouy B, Devred A. Evaluation of the transfer of heat from the coil of the LHC dipole magnet to helium II. IEEE Trans Appl Supercond 2007;17(2):1263–8. https://doi.org/10.1109/TASC.2007.898030.
[5] Allain H, Quintard M, Prat M, Baudouy B. Upscaling of superfluid helium flow in porous media. Int J Heat Mass Transf 2010;53(21):4852–64. https://doi.org/10.1016/j.ijheatmasstransfer.2010.06.007.
[6] Granieri PP, Baudouy B, Four A, Lentijo F, Mapelli A, Petagna P, et al. Steady-state heat transfer through micro-channels in pressurized He II. In: ADVANCES IN CRYOGENIC ENGINEERING: transactions of the cryogenic engineering conference - CEC, vol. 57. 2012. p. 231–8.
[7] Granieri PP. Heat transfer through cable insulation of Nb–Ti superconducting magnets operating in He II. Cryogenics 2013;53:61–71. https://doi.org/10.1016/j.cryogenics.2012.06.007.
[8] Lanza C, Perini D. Characteristics of the austenitic steels used in the lhc main dipoles. IEEE Trans Appl Supercond 2002;12(1):1252–5. https://doi.org/10.1109/TASC.2002.1018629.
[9] Bottura L. Magnet quench 101., workshop on accelerator magnet, superconductor, design and optimization, 15 - 16 jan 2013. Geneva, Switzerland: CERN; 2013. p. 1–9. arXiv:1401.3927.
[10] Bottura L, Calvi M, Siemko A. Stability analysis of the LHC cables. Cryogenics 2006;46(7):481–93. https://doi.org/10.1016/j.cryogenics.2006.01.012.
[11] Chorowski M, Pietrowicz S, Weelderen Rv. Towards a better understanding of the physics of the two-volume model of accelerator magnet quench thermohydraulics. Cryogenics 2006;46(7):581–8. https://doi.org/10.1016/j.cryogenics.2006.01.013.
[12] Granieri PP, Calvi M, Xydi P, Baudouy B, Bocian D, Bottura L, et al. Stability analysis of the LHC cables for transient heat depositions. IEEE Trans Appl Supercond 2008;18(2):1257–62. https://doi.org/10.1109/TASC.2008.922543.
[13] Bocian D, Dehning B, Siemko A. Modeling of quench limit for steady state heat deposits in LHC magnets. IEEE Trans Appl Supercond 2008;18(2):112–5. https://doi.org/10.1109/TASC.2008.921338.
[14] Chase CE. Thermal conduction in liquid helium II. I. Temperature dependence. Phys Rev 1962;127(2):361–70.
[15] Ahlers G. Mutual friction in He II near the superfluid transition. Phys Rev Lett 1969;22(2):54–6.
[16] Leiderer P, Pobell F. Critical currents in superfluid helium near T_λ. Z Phys Hadrons Nucl 1969;223(4):378–84.
[17] Bon Mardion G, Claudet G, Seyfert P. Practical data on steady state heat transport in superfluid helium at atmospheric pressure. Cryogenics 1979;19(1):45–7.
[18] Sato A, Maeda M, Kamioka Y. Normalized representation for steady state heat transport in a channel containing He II covering pressure range up to 1.5 MPa. In: Proceedings of the twentieth international cryogenic engineering conference (ICEC20). Elsevier; 2005. p. 849–52.
[19] Dresner L. Transient heat transfer in superfluid helium. In: Advances in cryogenic engineering, vol. 27. 1982. p. 411–9.
[20] Shiotsu M, Hata K, Hama K, Shirai Y. Transient heat transfer produced by a stepwise heat input to a flat plate on one end of a rectangular duct containing pressurized helium ii. Adv Cryog Eng 2000:1065–72.
[21] Baudouy B. Heat-balance integral method for heat transfer in superfluid helium. Therm Sci 2009;13(2):121–32. https://doi.org/10.2298/TSCI0902121B.
[22] Dresner L. Transient heat transfer in superfluid helium. Part II. Tech. Rep. USA: Oak Ridge National Lab., TN; 1983.
[23] Vitrano A, Baudouy B. Double phase transition numerical modeling of superfluid helium for fixed non-uniform grids. Comput Phys Commun 2022;273:108275. https://doi.org/10.1016/j.cpc.2021.108275.
[24] Caspi S, Frederking T. Triple-phase phenomena during quenches of superconductors cooled by pressurized superfluid helium II. Cryogenics 1979;19(9):513–6. https://doi.org/10.1016/0011-2275(79)90003-1.
[25] Breon S, Van Sciver S. Boiling phenomena in pressurized He II confined to a channel. Cryogenics 1986;26(12):682–91. https://doi.org/10.1016/0011-2275(86)90169-4.
[26] Vitrano A. Study of heat and mass transfer in superfluid helium in confined geometries. PhD thesis. Physique des Accélérateurs, Université Paris-Saclay; 2021. https://www.theses.fr/en/2021UPASP057.
[27] Claudet G, Aymar R. Tore supra and He II cooling of large high field magnets. Adv Cryog Eng 1990:55–67.
[28] Manganin®. Manganin - Resistance Alloy, Goodfellow Corporation, 125 Hookstown Grade Road, Coraopolis. PA 15108-9302.
[29] Tektronix®. Bench Power and DC Power Supply. Tektronix, Inc., Beaverton, Oregon.
[30] Cornwell K, Kew PA. Boiling in small parallel channels. Energy efficiency in process technology; 1993. p. 624–38.
[31] Capatina O, Poncet A, Skoczen B. Lambda front propagation in the superfluid helium contained in the external auxiliary bus-bar line of the LHC. AIP conference proceedings, vol. 710. American Institute of Physics; 2004. p. 1068–78.
[32] Sitko M, Skoczeń B. Modelling He I-He II phase transformation in long channels containing superconductors. Int J Heat Mass Transf 2009;52(1):9–16. https://doi.org/10.1016/j.ijheatmasstransfer.2008.06.009.